





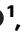



Integrating hydrogen utilization in CO₂ electrolysis with reduced energy loss

Received: 3 May 2023

Accepted: 5 February 2024

Published online: 16 February 2024

Xiaoyi Jiang ^{1,2}, Le Ke ^{1,2}, Kai Zhao ^{1,2}, Xiaoyu Yan ¹, Hongbo Wang ¹,
Xiaojuan Cao ¹, Yuchen Liu^{1,2}, Lingjiao Li ^{1,2}, Yifei Sun ³, Zhiping Wang ¹,
Dai Dang⁴ & Ning Yan ^{1,2} ✉

Electrochemical carbon dioxide reduction reaction using sustainable energy is a promising approach of synthesizing chemicals and fuels, yet is highly energy intensive. The oxygen evolution reaction is particularly problematic, which is kinetically sluggish and causes anodic carbon loss. In this context, we couple CO₂ electrolysis with hydrogen oxidation reaction in a single electrochemical cell. A Ni(OH)₂/NiOOH mediator is used to fully suppress the anodic carbon loss and hydrogen oxidation catalyst poisoning by migrated reaction products. This cell is highly flexible in producing either gaseous (CO) or soluble (formate) products with high selectivity (up to 95.3%) and stability (>100 h) at voltages below 0.9 V (50 mA cm⁻²). Importantly, thanks to the “transferred” oxygen evolution reaction to a water electrolyzer with thermodynamically and kinetically favored reaction conditions, the total polarization loss and energy consumption of our H₂-integrated CO₂ reduction reaction, including those for hydrogen generation, are reduced up to 22% and 42%, respectively. This work demonstrates the opportunity of combining CO₂ electrolysis with the hydrogen economy, paving the way to the possible integration of various emerging energy conversion and storage approaches for improved energy/cost effectiveness.

Electrocatalytic CO₂ reduction reaction (CO₂RR) at low temperatures is among the most promising approaches of sustainably producing fuels and chemicals^{1–3}. Tremendous progress regarding materials development, fundamental understandings and technological innovations have been made over the past decades, rendering high-rate and selective formation of products spanning from C1 (e.g., CO and CH₄) to C3 (e.g., propanol)^{4–12}. However, the high energy input and low energy efficiency remain a major barrier impeding the large-scale application in real life. Specifically, the oxygen evolution reaction (OER) at the anode is both energetically intensive and kinetically sluggish, yet generating diatomic oxygen with low market value^{13–17}. The oxygen production often causes carbon loss, further reducing the energy efficiency^{18–20}: the readily formed carbonate or bicarbonate

ions at the cathode can migrate, through either aqueous electrolyte or anion-exchange membrane (AEM), to the anode with a lower local pH value. Consequently, the protonation results in the release of CO₂ together with the evolved O₂. In a typical AEM based CO₂ electrolyzer, carbon loss caused by CO₂ crossover could reach ca.70%²¹. The energy penalty of recovering CO₂ using amine scrubbing is gigantic, ca. 3–7 GJ/tonne CO₂^{19,20}. Recent estimations show that this energy is even ~1.6 times more demanding than the electrolysis step^{20,21}.

In this context, the so-called “paired electrolysis” becomes a hot research topic, in which CO₂RR is coupled with a thermodynamically and/or kinetically more favorable half-reaction^{16,22–25}. Electro-oxidations of aldehyde, glycerol, ethanol, isopropanol, 1,2-propanediol and other organics have been identified as suitable OER

¹School of Physics and Technology, Wuhan University, Wuhan 430072, China. ²Shenzhen Research Institute of Wuhan University, Shenzhen 518057, China.

³Shenzhen Research Institute of Xiamen University, Shenzhen 518057, China. ⁴School of Chemical Engineering and Light Industry, Guangdong University of Technology, Guangzhou 510006, China. ✉e-mail: ning.yan@whu.edu.cn

substitutes, which indeed lower both energy input and overpotential loss while coproducing value-added products^{16,25–28}. Nonetheless, this strategy has two potential limitations: the prominent one is the huge market-size mismatch between the cathode and anode chemicals. For instance, the emitted CO₂ from the industry sector alone that can be captured and utilized is in gigatonne level per year, yet the annual market demand of nearly all products which can be potentially coproduced from the paired electrolysis is in (and often less than) the million-tonne scale^{29–31}. Moreover, the separation and purification of products from the electrolyte pose another challenge toward the practical application²⁴.

On the big picture of renewable energy storage, hydrogen is another major energy carrier for various downstream applications³². Pairing CO₂RR with hydrogen oxidation can theoretically address the abovementioned challenges while reducing the energy input. It should be noted that green hydrogen generation via water electrolysis also involves the OER which can occur at much more favored thermodynamic and kinetic conditions compared with that in CO₂RR reactors (e.g., neutral or weaker-alkaline electrolytes and lower operating temperatures)^{13,33–36}. For instance, the anodic overpotential loss in advanced solid oxide water electrolysis cell (SOEC) and alkaline water electrolyzer (AWE) is as low as 0.01 V and 0.2 V at 50 mA cm⁻², respectively; yet, it often exceeds 0.52 V in CO₂RR reactor at neutral conditions^{35,37}. One would imagine intuitively if we can “transfer” the OER in CO₂RR to water electrolyzer to boost the energy efficiency.

Inspired by the facts above, we proposed the direct coupling of CO₂ electrolysis with hydrogen oxidation reaction (HOR) at the anode in a single electrochemical cell. Using CO₂-to-CO and CO₂-to-formate as two model reactions to respectively represent the reactions yielding gaseous and electrolyte-soluble products, we showed the effectiveness and efficiency of such H₂-integrated CO₂RR. A flow cell with a Ni(OH)₂/NiOOH mediator was designed to prevent carbon loss and HOR catalyst poisoning by the migrated CO₂RR products; we also developed a gas-diffusion electrode with a gradient functional layer which minimized the cathodic overpotential loss. The kinetic advantages were discussed in comparison with conventional systems. Importantly, our H₂-integrated CO₂RR, coupled with either AWE or SOEC, promised to decrease the total energy consumption up to 42%.

Results

Theoretical considerations and cell design

Figure 1a shows the conventional CO₂RR process in comparison with the H₂-integrated CO₂RR combining with water electrolysis. The problematic OER is transferred to a water electrolyzer, potentially alleviating the high energy consumption in conventional CO₂RR brought by carbon loss and high OER overpotential. Note that pairing CO₂ with HOR is also practically feasible in terms of “mass balance”: assuming 100 million tonnes of stored H₂ (approximately the global H₂ production in 2021) is used to convert CO₂ to CO, 2.2 gigatonnes of CO₂ can be stoichiometrically utilized, accounting for ~25% of global CO₂ emissions from the industry sector in 2022 according to the

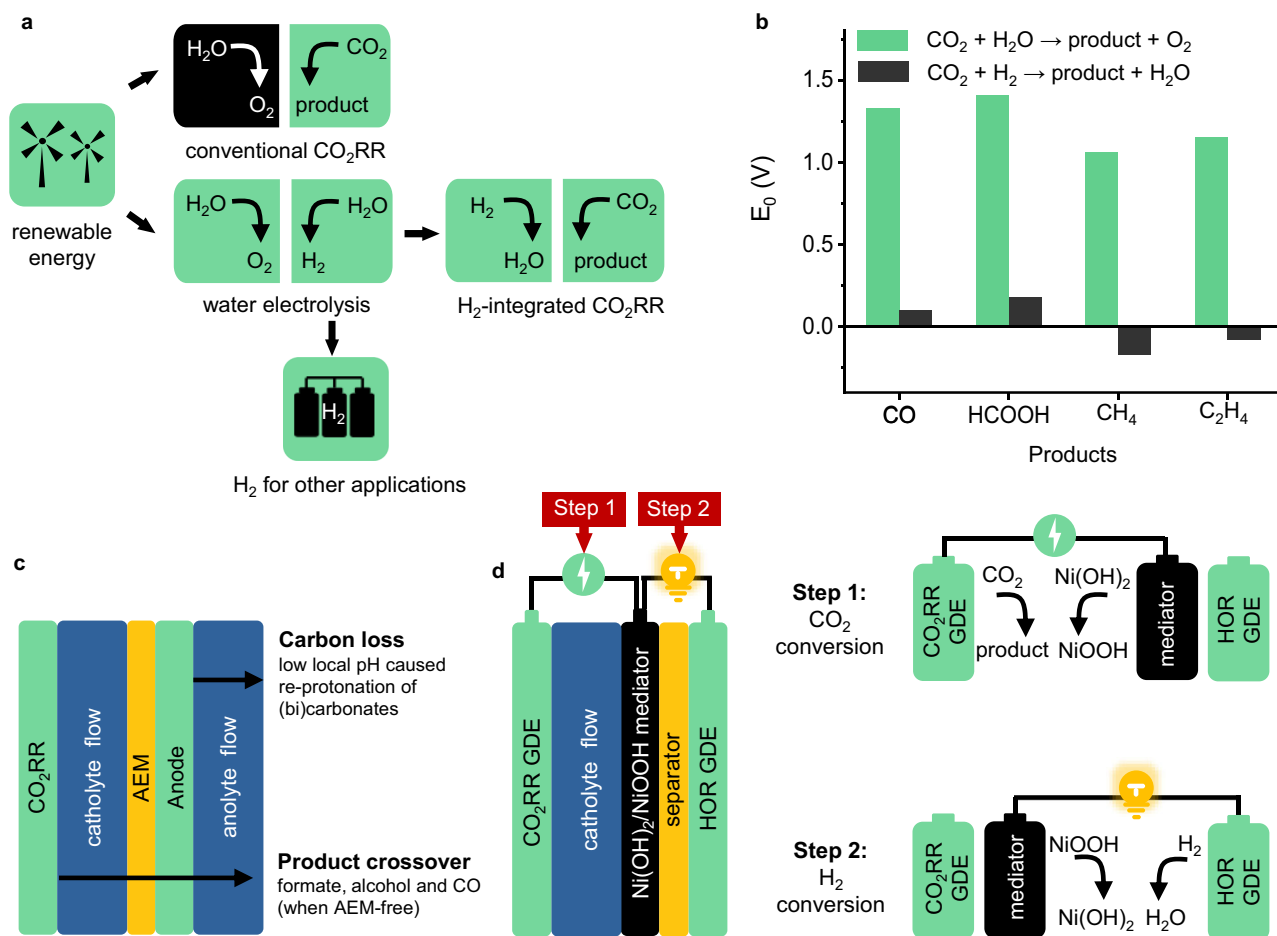


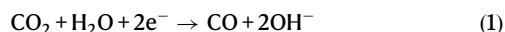
Fig. 1 | H₂-integrated CO₂RR and the cell configuration. **a** Illustrative comparison of H₂-integrated and conventional CO₂RR; **b** Comparison of Nernst potentials (E_0) between conventional and H₂-integrated CO₂RR; **c** Potential carbon loss and

product crossover at the anode side in a typical CO₂ flow electrolyzer; **d** Cell configuration and detailed working principles of the H₂-integrated CO₂RR cell.

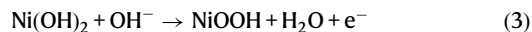
International Energy Agency (IEA). Figure 1b compares the Nernst potentials of conventional and H₂-integrated CO₂RR at standard conditions in four typical conversions. Reactions toward CO and formic acid remain electrolytic in H₂-integrated CO₂RR, yet the Nernst potentials drop to only 0.10 and 0.18 V, respectively. Reactions toward CH₄ and C₂H₄ are even more promising, as the potentials respectively decrease to -0.17 and -0.08 V, implying that these conversions can theoretically generate electricity (see Supplementary Table 1 in the Supplementary Information for details). One would envisage that using a classic flow reactor or a membrane electrode assembly (MEA) would realize this concept. But there are at least two catches as shown in Fig. 1c: (1) the low local pH at the anode will lead to the re-protonation of migrated (b)carbonate ions and the release CO₂ gas. It mixes with the residual H₂ in the anode effluent, causing significant CO₂ loss; (2) CO₂RR products such as CO (when membrane-free), formate and alcohols can migrate through the (membrane) electrolyte, potentially deactivating HOR catalysts (*vide infra*).

To achieve effective and efficient H₂-integrated CO₂RR, we designed a single cell with the detailed configuration shown in Fig. 1d and examined its effectiveness by performing H₂-integrated CO₂-to-CO and CO₂-to-formate as two model reactions. The cell contains a Ni(OH)₂/NiOOH mediator, sandwiched by a CO₂RR gas diffusion electrode (GDE) and a HOR GDE, to decouple CO₂RR and HOR while eliminating the sluggish oxygen catalysis. The working principle of the cell contains temporally and spatially separated Step 1 and Step 2, featuring an alternating operating sequence. Step 1 is for CO₂ conversion in which CO₂ is reduced to CO or formate at CO₂RR GDE and Ni(OH)₂ is oxidized to NiOOH as shown in Eqs. (1)–(5):

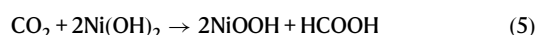
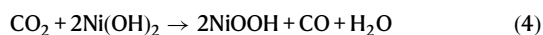
cathode:



anode:



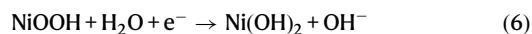
overall:



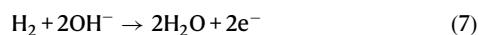
Compared with OER half reaction, the oxidation of Ni(OH)₂ is a single-electron transfer process with much lower overpotential loss (*vide infra*).

After the consumption of Ni(OH)₂, Ni electrode then works together with HOR GDE in Step 2 for energy harvesting with reactions shown below in Eqs. (6)–(8):

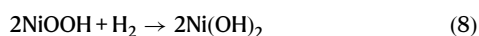
cathode:



anode:



overall:



This step is the typical reaction in a Ni-H₂ battery, generating electricity to partially compensate the power consumed in Step 1. The continuous operation of the system is enabled by the periodical swap between Step 1 and Step 2.

Reaction kinetics of electrodes

In the CO₂-to-CO model reaction, we used Zn nanosheet, prepared by electrodeposition, as the catalyst^{38–40}. The electrodeposition time is regulated ($t = 0$ s, 100 s, 500 s, and 1000 s) and the resulting samples are donated as Cu, Zn-Cu-100, Zn-Cu-500, and Zn-Cu-1000, respectively. The X-ray diffraction (XRD) pattern of Cu foam (Fig. 2a) shows characteristic diffraction peaks of pure metallic Cu (JCPDS No.04-0836). The extra peaks at 42.8° and 48.7° are attributed to Cu₂O (JCPDS No.05-0667) and CuO (JCPDS No.48-1548), respectively, as Cu is readily oxidized in ambient air. After Zn electrodeposition, two new peaks located at 36.3° and 38.9° appear, which are assigned to metallic Zn (JCPDS No.87-0713). Their intensity increases with the electrodeposition time because of the increased Zn loading (see Supplementary Table 2). The scanning electron microscopy (SEM) images show that all the deposited Zn has a nanosheet structure (see Fig. 2c and Supplementary Fig. 1b–d). The thickness of these nanosheets increases from 3 to 5 nm for Zn-Cu-100 to ca.50 nm for Zn-Cu-1000. The length of each sheet also grows from ~100 nm for Zn-Cu-100 to ~1.5 μm for Zn-Cu-1000.

The CO₂RR activity of as-synthesized electrocatalysts was first evaluated in a classic H-cell using CO₂-saturated 0.1 M KHCO₃ as the electrolyte. The linear sweep voltammetry (LSV) of Cu foam electrode shows a low current density, implying low CO₂RR activity (see Supplementary Fig. 2). Zn electrodeposition leads to increased current densities. The highest current density is achieved on Zn-Cu-500 electrode, which is mainly attributed to the largest surface area (Zn-Cu-100: 9.9208 m² g⁻¹; Zn-Cu-500: 25.6896 m² g⁻¹; Zn-Cu-1000: 24.3713 m² g⁻¹, see nitrogen adsorption-desorption isotherms in Supplementary Fig. 3). The smaller surface area of Zn-Cu-1000 could be ascribed to the “overgrowth” of Zn nanosheets as evidenced by SEM images. Pore size distribution analysis in Supplementary Fig. 4 confirms that Zn-Cu-500 also has the largest pore volume of 0.035 cm³ g⁻¹. The electrochemical surface areas (ECSAs) are consistent with these results, as the largest ECSA comes from Zn-Cu-500 (see Supplementary Figs. 5 and 6).

CO₂RR products from these catalysts were monitored during potentiostatic electrolysis in the potential window ranging from -0.5 to -1.1 V (vs. RHE and hereafter). Zn catalysts show completely different behaviors in comparison with Cu foam (see Fig. 2d and Supplementary Figs. 7 and 8 for details). In particular, Zn-Cu-500 exhibits the highest Faradaic efficiency (FE) toward CO formation (85.8% at -1.0 V, also see Supplementary Figs. 7 and 8), while the partial current density for CO (j_{CO}) reaches ca. 11 mA cm⁻² (see Fig. 2e). This performance is comparable with the state-of-the-art CO-selective catalysts synthesized using sophisticated approaches^{38,40}. Further decreasing the applied potential, however, leads to a drop of CO FE, which is attributed to mass-transport limitations at high current densities. The activity difference among three catalysts pertains to the variance of number of active sites rather than the change of intrinsic activity, since the surface-area-normalized current densities at low overpotentials for all catalysts are similar (see Supplementary Fig. 9). Note that the normalized current density for Zn-Cu-500 at high overpotentials was lower than that of Zn-Cu-100. This suggests that the complex nanostructure, while offering higher surface area and more active sites, might have mass transfer problems.

In the CO₂-to-formate model reaction, we also utilized a nanostructured electrocatalyst based on Bi₂O₃. In the hydrothermal synthesis, porous carbon nanospheres are added as the template on which Bi species are deposited. A final calcination step burns away carbon templates and converts Bi species into Bi₂O₃ porous nanospheres (see characterization results in Supplementary Fig. 10). This catalyst is

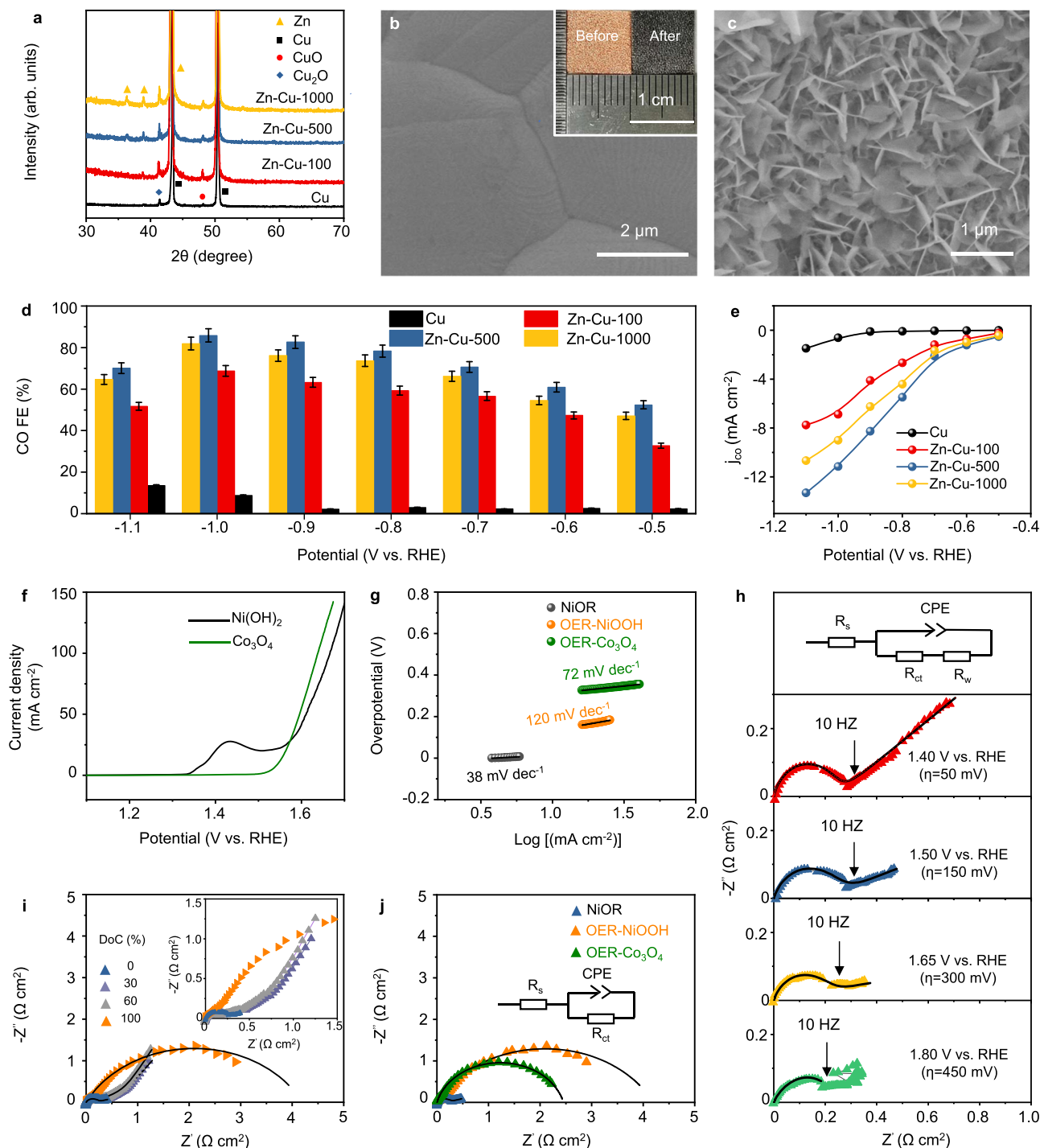


Fig. 2 | Characterizations and performance of Zn and Ni(OH)₂/NiOOH electrodes. **a** XRD patterns; SEM images of **b** Cu foam and **c** Zn-Cu-500, the inset compares the optical images of Cu foam before and after Zn deposition; **d** Potential-dependent Faradaic efficiency for CO generation (the error bar represents standard deviation from three independent measurements); **e** Plots of j_{CO} as a function of potential bias during CO₂RR; **f** LSV curves of Ni(OH)₂ and Co₃O₄ electrodes (the solution resistance was 1.25–1.35 Ω); **g** Tafel plots of NiOR and OER; **h** Nyquist plots of Ni(OH)₂ electrode acquired at 1.40, 1.50, 1.65, and 1.80 V vs. RHE; **i** Nyquist plots

of Ni(OH)₂/NiOOH electrode acquired at different DoC at 1.55 V vs. RHE, charging is defined as the Ni(OH)₂-to-NiOOH conversion; **j** Nyquist plots measured at 1.55 V vs. RHE of Ni(OH)₂/NiOOH electrode (DoC = 0% and =100%) and Co₃O₄. All solid black lines in Nyquist plots represent the fitting results based on the equivalent circuit, where R_s is the solution resistance, CPE is the constant phase element, R_{ct} is the charge-transfer resistance and R_w is the Warburg impedance. Source data are provided as a Source Data file.

highly selective to yield formate in the potential range from –0.45 to –1.05 V. The top formate FE reaches 89.0% at –0.65 V as shown in Supplementary Figs. 11 and 12.

We also examined the reaction kinetics of Ni(OH)₂/NiOOH mediator. Although its electrochemical behaviors in strong alkaline media

are well documented in the literature^{41–44}, the performance in weaker base, particularly in comparison with OER, is rarely reported. In the cyclic voltammogram (CV) shown in Supplementary Fig. 13, the redox peaks, corresponding to the Ni²⁺/Ni³⁺ conversion, are clearly observable. The onset potential of OER is ~220 mV higher than that of

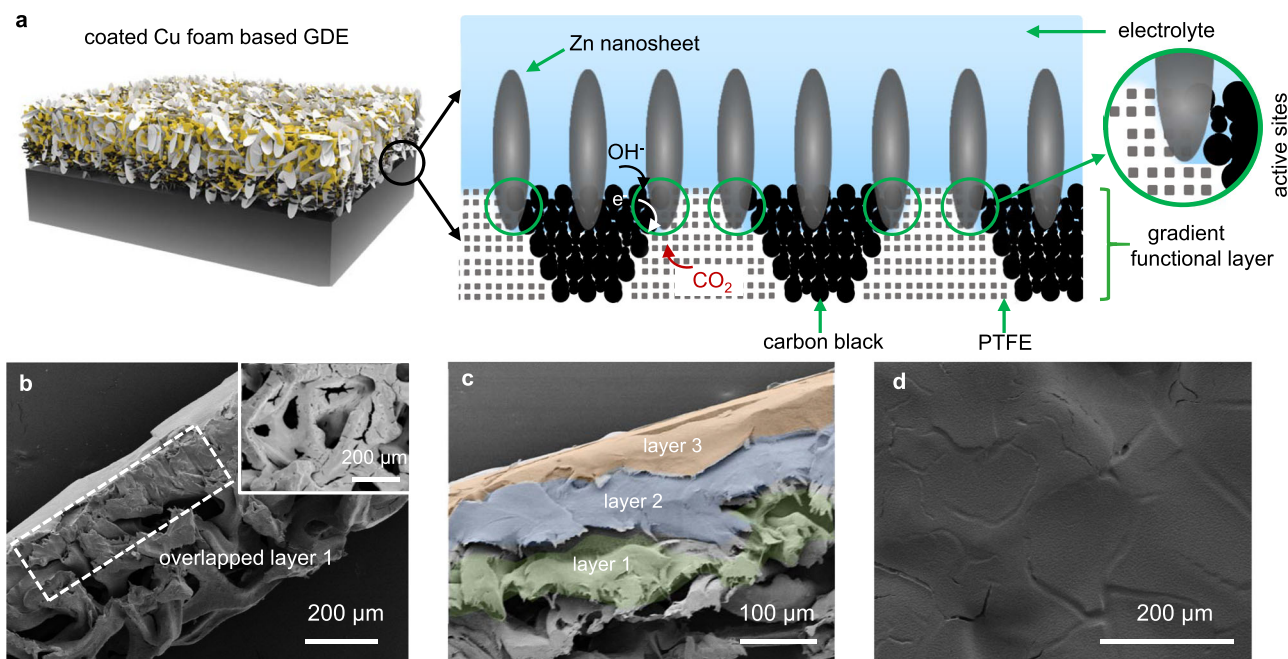


Fig. 3 | Characterizations of GDE based on the Zn-coated Cu foam. **a** The schematic illustration of GDE; cross-sectional SEM images of **b** merged foam with

carbon-PTFE layer after drop-casting the first layer (inset shows the surface image) and **c** final gradient functional layer; **d** SEM image of the top layer surface.

Ni(OH)₂ oxidation reaction (NiOR). As the Nernst potential of NiOR is higher than that of OER, the lower onset potential suggests the much-favored reaction kinetics as OER is a concerted four-electron-proton transfer process. This conclusion is also valid when comparing with a state-of-the-art OER catalyst, namely, nanostructured Co₃O₄ (detailed materials characterizations and OER performance are shown in Supplementary Fig. 14)⁴⁵, since NiOR shows lower onset potential and Tafel slope (see Fig. 2f, g).

The dynamic behaviors of Ni(OH)₂ electrode during NiOR are further examined using electrochemical impedance spectroscopy (EIS). The Nyquist plots, together with the fitting results, in Fig. 2h reveal charge-transfer kinetics at various potentials. Both the charge-transfer resistance (R_{ct}) and the Warburg impedance (R_w) decrease progressively when the potential bias increases from the open-circuit potential (OCP) to 1.65 V vs. RHE, implying that the NiOR kinetics is controlled by both charge transfer and mass transfer. Note that further increasing the potential bias causes the rise of R_{ct} due to the initiation of OER (also see Supplementary Table 3). The composition of Ni(OH)₂ electrode also affects reaction kinetics. In the Nyquist plots where the depth-of-charge (DoC) of Ni(OH)₂ varies (see Fig. 2i and Supplementary Table 4, charging is defined as Ni(OH)₂-to-NiOOH conversion), R_{ct} remains essentially identical when DoC is 0%, 30% and 60%. However, it drastically increases from 0.20 Ω to 4.19 Ω cm² when DoC reaches 100%, implying that the charge transfer process was then dominated by OER. Compared with the R_{ct} of OER on either NiOOH or Co₃O₄, the R_{ct} of NiOR is more than an order of magnitude smaller as shown in Fig. 2j and Supplementary Table 5. We also characterized the reverse process, i.e., NiOOH reduction reaction (NiRR), as shown in Supplementary Fig. 15. It seems that the diffusion process becomes the rate-limiting step: when the overpotential increases, R_{ct} remains nearly constant while R_w shows substantial rise (see Supplementary Table 6).

In the steady-state study using chronopotentiometric method (± 10 mA cm⁻²), stable redox reactions are observed in Supplementary Fig. 16. The high reversibility of Ni electrode in weak KOH electrolyte is also reflected by the roughly identical charge (ca. 200 C) stored/released in the reactions. The calculated Coulombic efficiency is >99%. Before the complete consumption of Ni(OH)₂ in the oxidation cycle, oxygen bubbles are hardly observable, implying that a simultaneous

and active OER is unlikely (*cf.* EIS spectra with different DoC and additional experimental proof below). Bubbles starts to appear when all Ni(OH)₂ is converted into NiOOH (see the comparison in the inset of Supplementary Fig. 16), accompanied by a sudden potential increase from 1.45 to 1.54 V. Hence we confirm that Ni(OH)₂/NiOOH mediator could perform well in weak alkaline electrolyte.

Cell performance

The detailed cell assembly for H₂-integrated CO₂RR is shown in Supplementary Fig. 17. Bi₂O₃ catalyst can be easily incorporated into the conventional carbon based GDE via infiltration. However, transforming Zn-Cu-500 foam into a GDE is not such straightforward. We thus developed a gradient functional layer, as illustrated in Fig. 3a, which was fabricated via a “layer-by-layer” method to form the GDE where the maximized amounts of active sites, effective mass transport and adequate mechanical strength with good conductivity are guaranteed concurrently. The gradient microstructure contains gas diffusion channels in the polytetrafluoroethylene (PTFE) phase and ion/electron transport pathways (carbon phase), which enables effective “inward” transport of CO₂ and “outward” transport of electrolyte to the active sites. In addition, it simultaneously allows lower contact resistance with the Zn-Cu-500 foam (due to higher content of carbon in the inner layer) and sufficient mechanical strength (due to higher content of PTFE in the outer layer). The gradient functional layer partially overlaps with the porous foam because of the slurry-drop-casting fabrication technique. The electrochemically active sites, where Zn nanosheets share common areas with carbon, PTFE and aqueous electrolyte, are thus created to include more Zn nanosheets.

The SEM images confirm the successful preparation of the gradient functional layer in the GDE. Figure 3b demonstrates the cross-sectional image of Zn-Cu-500 foam after applying the first layer. It seems that all the drop-casted carbon-PTFE composite stays inside the porous structure without forming an intact surface film (see the inset in Fig. 3b). After applying another two layers with varied carbon-PTFE ratios, a robust, dense and water-proof film finally appears on the top. Neither delamination among layers nor cracks/pores on the surface is observed in the SEM images in Fig. 3c, d and Supplementary Fig. 18. Moreover, XRD patterns of GDE indicate the phase stability of Zn

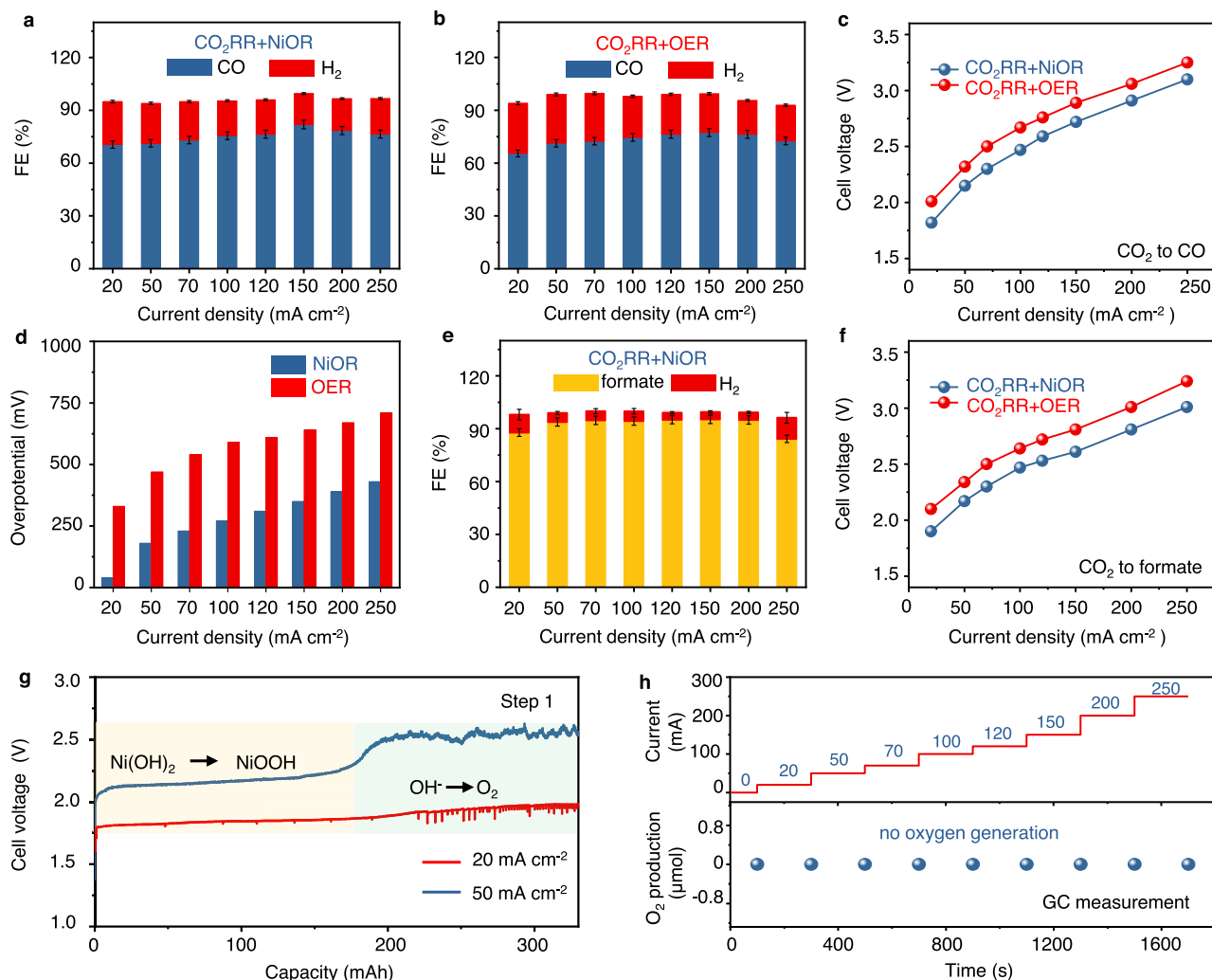


Fig. 4 | Cell performance in CO₂RR. Faradaic efficiencies of CO production in **a** CO₂RR + NiOR and **b** CO₂RR + OER; **c** Polarization curve comparison of CO₂RR + NiOR and CO₂RR + OER for CO production; **d** Anode overpotentials of NiOR and OER during CO₂RR at different current densities; **e** Faradaic efficiencies of formate production in CO₂RR + NiOR; **f** Polarization curve comparison of

CO₂RR + NiOR and CO₂RR + OER for formate production; **g** Chronopotentiometry curves of Step 1 (CO₂RR + NiOR) for CO production at 20 and 50 mA cm⁻²; **h** O₂ production at the anode in Step 1 at different current densities. The error bar represents standard deviation from three independent measurements. Source data are provided as a Source Data file.

during the heat treatment when fabricating the electrode (see Supplementary Fig. 19).

We then applied both Zn- and Bi₂O₃-based GDE in our cell to examine the H₂-integrated CO₂RR. In Step 1 for CO₂ reduction to CO, the FE of CO is comparable with that obtained in the H-cell, implying the effectiveness of Zn based GDE with a gradient functional layer (see Fig. 4a). The maximum CO FE reached 81.9% at 150 mA cm⁻², more details including CO FE, cell voltages, cathodic potentials, and anodic potentials at 20–250 mA cm⁻² are listed in Supplementary Table 7. Note that the sum of FEs for both CO and H₂ is not 100% as the soluble products in the flowing electrolyte are not analyzed.

In the control experiment where NiOR is replaced by OER at the anode using Co₃O₄ catalyst, the observed CO FE is similar with our Step 1 process at all current densities (see Fig. 4b and Supplementary Table 8). This result indicates that the substitution of OER by NiOR has no influence on the cathodic reaction, which is further supported by the essentially identical overpotentials monitored at the cathode (see Supplementary Fig. 20). Importantly, the cell voltages of Step 1 are 0.15–0.20 V lower than the conventional processes at all current densities (see Fig. 4c, Supplementary Figs. 21 and 22). By respectively monitoring the cathodic and anodic overpotentials, we conclude that this voltage decrease is ascribed to the replacement of OER by NiOR as

shown in Fig. 4d. For example, the overpotential of OER is 330 mV at 20 mA cm⁻², yet is only 40 mV for NiOR. Indeed, OER is thermodynamically more favorable with lower standard reduction potentials (0.40 vs. 0.49 V for NiOR). But the coupled transfer of 4 electrons and 4 protons makes OER kinetically sluggish. The evolution of molecular oxygen gas may also cause additional overpotential loss due to mass transport. Conversely, NiOR is a single-electron/proton transfer process without gas evolution.

Similarly, in Step 1 for CO₂RR to formate using Bi₂O₃ based GDE, the maximum formate FE tops ~95.3% at 150 mA cm⁻² (see Fig. 4e, Supplementary Fig. 23 and Supplementary Table 9 for details). The cell voltages are 0.17–0.23 V lower than the conventional processes at the same current densities (see Fig. 4f). This difference is also due to the kinetic advantage of NiOR as discussed above (see Supplementary Fig. 23, Supplementary Tables 9 and 10). We thus infer that our cell architecture, together with the paired NiOR, is flexible and effective in enhancing voltage efficiency for reactions toward both gaseous (CO) and soluble (formate) products. The steady-state study for an extended period is also performed. Figure 4g shows the example for CO generation. At 20 mA cm⁻², the average electrolysis voltage is only 1.85 V, corresponding to a voltage efficiency of 78.4% (see Supplementary Note 1). At 50 mA cm⁻², this voltage increases to 2.15 V;

the full conversion of Ni(OH)₂ is indicated by a sharp voltage rise to 2.52 V, implying the start of OER. Continuous operation of CO₂RR must incorporate H₂ oxidation in Step 2 which is discussed below.

Albeit that CO₂ crossover from cathode to anode remains possible in the new cell during CO₂RR, the readily formed CO₂ gas can be retrieved easily at the anode side if no oxygen forms during NiOR. We thus used online gas chromatography (GC) to monitor the anode affluent in which no oxygen has been detected (see Fig. 4h). Note that to facilitate the gas collection at the anode while maintaining electrolyte flow at the cathode, we slightly modified the cell by placing an anion-exchange membrane to separate the anode and cathode compartment (see details in the SI and Supplementary Fig. 24). This modification also suggests that our cell is flexible with both membrane-free and membrane-based configurations. The absence of OER at the anode is also supported by the in-situ differential electrochemical mass spectrometry (DEMS) measurement in which Ni(OH)₂ was used as the working electrode biased at various constant current densities (see details in the SI and Supplementary Fig. 25)⁴⁶. No O₂ signal (*m/z* = 32) is detected in the current density ranging from 0 to 70 mA cm⁻² (280 mA cm⁻² equivalent in the cell) for pristine Ni(OH)₂ electrode. Further study indicates that the oxygen formation is also affected by the DoC of Ni(OH)₂ electrode. When DoC is below 20.8%, oxygen is undetectable below 150 mA cm⁻² equivalent (see Supplementary Figs. 26 and 27). When the applied current density is below 40 mA cm⁻² equivalent, no OER occurs even when DoC reaches >90%.

After full conversion of Ni(OH)₂ to NiOOH in Step 1, hydrogen utilization and energy harvesting is then conducted in Step 2. As a proof-of-concept, we used Pt/C GDE for HOR without developing a new catalyst. The electrolyte is switched to 6 M KOH to minimize polarization losses. The maximum power density in Fig. 5a reaches 221 mW cm⁻² which is comparable with the state-of-the-art Ni-H₂ and Zn-air batteries^{47,48} (see Supplementary Fig. 28). In the control experiment, we tested CO₂RR with HOR simultaneously occurring at the anode without using Ni(OH)₂/NiOOH mediator (see the cell structure in Supplementary Fig. 29). The polarization curve from the very first scan indeed shows substantially lower operating voltage. Yet, in the 2nd and 3rd run, performance deteriorates as the voltage sharply increases to values that are similar to the conventional CO₂RR (Fig. 5b). This phenomenon is aligned with the steady-state electrolysis in which a sudden voltage or current density degradation is observed after a period of time (see Supplementary Fig. 30). We analyzed the spent HOR electrode using the Fourier transformed infrared spectroscopy (FTIR) as a function of electrolysis time. A wide band at ca. 2100–2000 cm⁻¹, which corresponds to atop adsorbed CO species on Pt⁴⁹, starts to appear after ~300 s (see the inset of Fig. 5b). We thus ascribe the degradation to CO poisoning of Pt electrode. Additionally, formate, methanol and ethanol could deactivate Pt too as shown in Supplementary Fig. 31. These CO₂RR products can migrate through the liquid electrolyte or AEM, occupying the active sites for hydrogen oxidation⁵⁰. Therefore, Ni(OH)₂/NiOOH mediator is indeed necessary and effective in tackling both carbon loss and HOR catalyst poisoning.

The steady-state study of Step 2 at galvanostatic conditions is shown in Fig. 5c. At 20 and 50 mA cm⁻², the cell voltage is ~1.28 V, comparable with the state-of-the-art Ni-H₂ batteries. The voltage efficiency is higher than 95%, which outperforms that of the proton-exchange membrane fuel cell (PEMFC) in our own test and in the literature (see Supplementary Fig. 32 and Supplementary Table 13)⁵¹. Combined with the data in Step 1, we find the Coulombic efficiency of the mediator is >99%. Figure 5d shows the periodical swap between Step 1 and Step 2 at different current densities. While relatively stable voltages are recorded from 20 to 150 mA cm⁻², the voltage efficiencies, for both CO and formate generation in Fig. 5e, decrease when the current density rises. In the multi-swap test, we select 50 mA cm⁻² as the benchmark for both Step 1 and Step 2. In the CO₂-to-CO conversion shown in Fig. 5f, the operation time of each cycle is set at 2000 s, a

shallow charge-discharge profile can extend the lifespan of typical Ni electrode to tens of thousands of cycles^{44,47}. After 10 full cycles, no degradation is observed and the CO FE remains at 72 ± 1%. In the 100 h longevity test for both CO₂-to-CO and CO₂-to-formate conversion as shown in Supplementary Figs. 33 and 34. The voltage degradation remains trivial, which only comes from Step 1 (0.11 V and 0.12 V for CO and formate generations, respectively). The spent Zn and Bi₂O₃ GDEs show unchanged microstructures in the SEM. In particular, the gradient functional layer of the Zn GDE remains intact, no cracks or delamination is seen in SEM images shown in Supplementary Figs. 35 and 36. No CO contaminant is detected on Pt/C GDE after longevity test (see Supplementary Fig. 37).

Energy efficiency and techno-economic analyses are finally carried out in comparison with the conventional CO₂RR. We first used “operating voltage” as the descriptor which directly reflect the energy consumption at a fixed current, H₂-integrated CO₂RR shows 0.87 V and 0.89 V cell voltage at 50 mA cm⁻² (defined as the voltage difference between Step 1 and Step 2) for CO and formate generations, respectively. They are significantly lower than the conventional counterparts and the state-of-the-art in the literature (with and without paired oxidation reactions, see Fig. 5g and Supplementary Table 12). To evaluate the energy efficiency of H₂-integrated CO₂RR where the upstream hydrogen generation should be included too, we constructed an AWE and an electrode-supported SOEC (see the SI for all technical details, Supplementary Figs. 38–40) which are representative approaches of today’s green hydrogen production. Their polarization curves for water electrolysis are shown in Supplementary Figs. 38 and 40. We also select 50 mA cm⁻² as the benchmark current density at which SOEC and AWE deliver cell voltages of 0.94 and 1.43 V, respectively. Thus, the equivalent operating voltages of H₂-integrated CO₂RR + SOEC and H₂-integrated CO₂RR + AWE are 1.81 and 2.30 V for CO₂RR-to-CO conversion, respectively, both of which are lower than that of conventional CO₂RR (2.32 V). A detailed half-reaction overpotential (η) analysis is shown in Fig. 5h and Supplementary Table 11. Interestingly, OER alone in conventional CO₂RR reaches η = 0.47 V, much higher than the sum of all losses in SOEC, Ni mediator and HOR in Step 2 in the H₂-integrated CO₂RR + SOEC (η_{sum} = 0.26 V). It is also higher than the η_{sum} for H₂-integrated CO₂RR + AWE (0.44 V). Same conclusion is also drawn in the CO₂RR-to-formate conversion. These results imply the kinetic benefits of transferring OER in CO₂RR to a water electrolyzer.

We also use energy consumption (GJ) per tonne of product as the performance descriptor (see Fig. 5i and Supplementary Note 2). Interestingly, the H₂-integrated CO₂RR coupled with water electrolysis (SOEC or AWE), despite of the higher level of system complexity, demonstrates up to 23% reduction in energy consumption. For instance, conventional CO₂RR requires 22.4 GJ to produce one tonne of CO whereas H₂-integrated CO₂RR + AWE needs 22.2 GJ; the SOEC-involved system is even more advantageous (17.5 GJ). When the anodic CO₂ recovery energy is considered in neutral conditions, both AWE and SOEC-coupled H₂-integrated CO₂RR demonstrate ample efficiency advantages, showing 27% ~ 42% decrease in energy consumption. This conclusion is also verified at various operating conditions (see Supplementary Tables 14–19). Indeed, direct CO₂-to-CO conversion in SOEC consumes even less energy (e.g., ~13.5 GJ⁵²), but the low-temperature CO₂ electrolysis enjoys the capability of generating various C1–C3 products. In the preliminary techno-economic analysis, we use an established model by considering a pilot plant producing 100 tonne of CO per day⁵³. Not surprisingly, the materials expense of our single H₂-integrated CO₂RR cell is higher than the conventional counterpart due to the use of mediator and the incorporation of an advanced water electrolyzer (see Supplementary Note 3 and Supplementary Fig. 41). Such additional capital expenditure can be compensated since the plant can behave as a battery energy storage system and can produce hydrogen too, offering versatile solutions for the market.

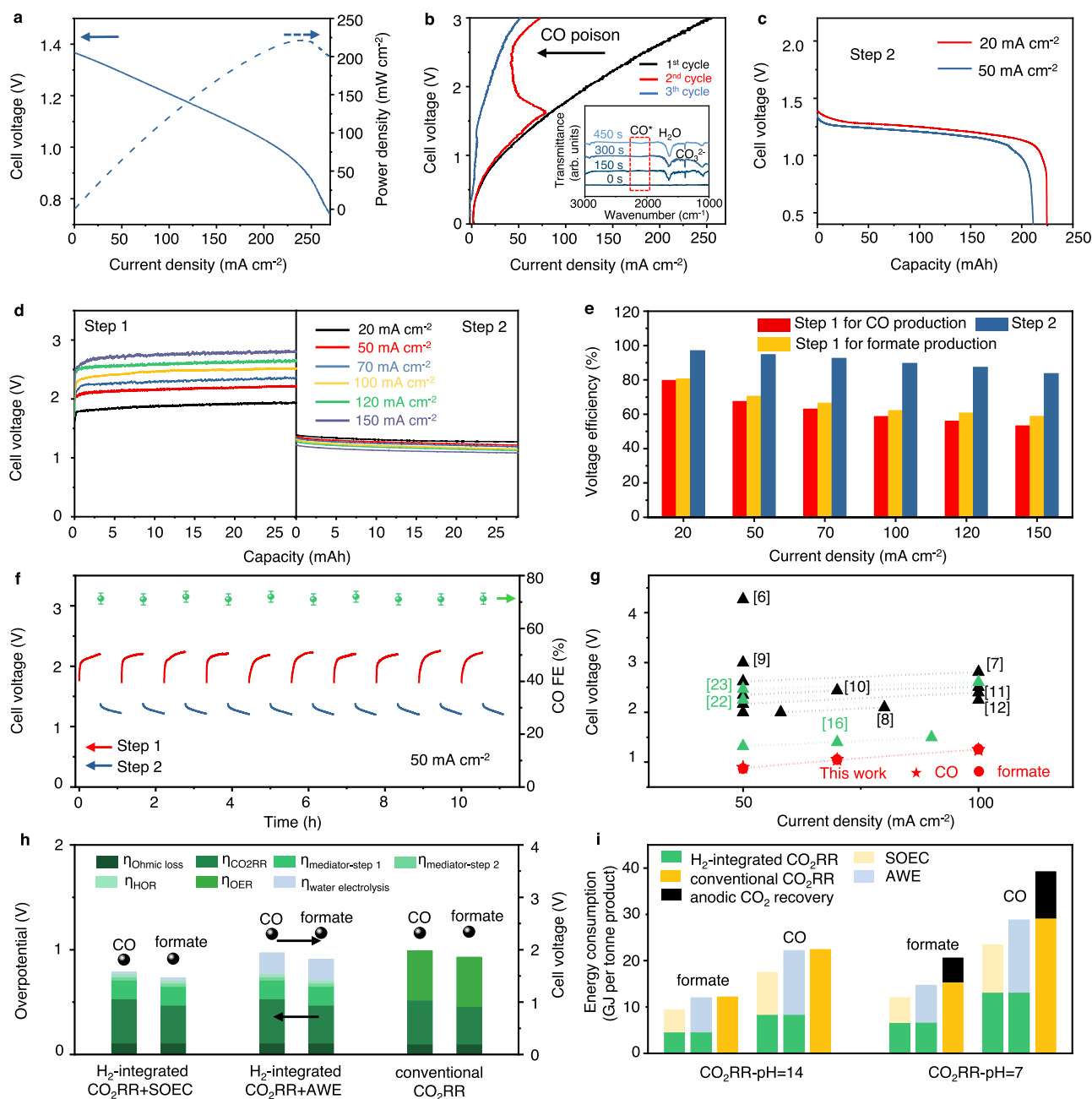


Fig. 5 | Cell performance in hydrogen conversion and the overall performance assessment. **a** Polarization and power density curves of Step 2; **b** Polarization curves of CO₂RR directly coupling anodic HOR, the inset shows the FTIR spectroscopy of Pt/C GDE during the HOR process; **c** Chronopotentiometry curves of Step 2 at 20 and 50 mA cm⁻²; **d** Swap between Step 1 and Step 2 for CO generation; **e** Voltage efficiency of Step 1 and Step 2; **f** Multi-swap test between Step 1 and Step 2 at 50 mA cm⁻² for CO generation; **g** Comparison of operating voltages of

H₂-integrated CO₂RR and state-of-the-art CO₂RR in the literature with (green) and without (black) paired electrooxidations from refs. 6–12,16,22,23; **h** Contributions of polarization losses in H₂-integrated CO₂RR coupled with water electrolyzers and in conventional CO₂RR at 50 mA cm⁻²; **i** Comparison of energy consumptions between H₂-integrated CO₂RR coupled with water electrolyzer and conventional CO₂RR at 50 mA cm⁻², assuming CO₂ recovery costs 4 GJ per tonne of CO₂ [20]. Source data are provided as a Source Data file.

Discussion

We have successfully developed a single electrochemical CO₂RR cell pairing H₂ oxidation at the anode. The operating voltage of the cell is substantially decreased to <0.9 V at 50 mA cm⁻². The use of a Ni(OH)₂/NiOOH mediator to decouple the electrode reaction effectively mitigates HOR catalyst poisoning while prohibiting anodic carbon loss. Even by including the energy input of hydrogen generation, we found the H₂-integrated CO₂RR can cut the total energy consumption by 42% thanks to the transferred OER to a water electrolyzer with favored reaction conditions. We

envisage that the direct coupling of CO₂RR and HOR without using a redox mediator is more promising which can further cut the energy input by 2.0 GJ per tonne of CO. Thus, finding effective approach of tackling CO₂ crossover in neutral conditions and developing poisoning-resistant HOR catalyst becomes critical. While this work demonstrates the opportunity of combining CO₂RR with grid-scale energy storage, it might also inspire the community to consider the integration of various emerging energy conversion and storage approaches with the aim of maximizing the energy efficiency.

Methods

Preparation procedures of electrodes

Preparation of Zn-Cu electrode. Zn nanosheet on Cu foam was prepared by electrodeposition. The aqueous electrolyte solution contained 1.5 M $(\text{NH}_4)_2\text{SO}_4$ and 0.1 M $\text{ZnSO}_4 \cdot 7\text{H}_2\text{O}$. Before electrodeposition, Cu foam was washed by diluted HCl solution for 5 min, and sequentially rinsed by deionized (DI) water for three times. The deposition was performed at a geometric current density of 4 mA cm^{-2} for different periods of time. To prepare the foam-based GDE, we first immersed the cleaned Zn-Cu foam ($2 \times 2 \text{ cm}^2$) in 10 wt.% polytetrafluoroethylene (PTFE) dispersion (Shanghai Aladdin Biochemical) for 30 s to form a hydrophobic layer on the surface which facilitated the fabrication of the gradient functional layer in the subsequent steps. The carbon-PTFE suspension was prepared by mixing 0.1 g carbon black with different volume of PTFE dispersion via sonication. The carbon ratio to PTFE was 80 wt.%, 50 wt.%, and 20 wt.% (denoted as C-PTFE-80, C-PTFE-50, C-PTFE-20, respectively). To prepare the gradient functional layer, we used a “layer-by-layer” technique via drop-casting 0.5 mL C-PTFE-80 dispersion first on the Zn-Cu foam. The as-prepared electrode was dried in air and then heat-treated in N_2 at 350°C for 30 min. Then, C-PTFE-50 and C-PTFE-20 layer was sequentially deposited using the identical method. In the final structure, each layer was ca. 50–75 μm thick.

Preparation of Bi_2O_3 electrode. The porous Bi_2O_3 nanosphere was prepared by a hydrothermal synthesis using a template method. To obtain the carbon template, 60 mL of 0.55 M glucose solution was added and sealed in a 100 mL Teflon-lined autoclave, followed by a hydrothermal reaction at 200°C for 4 h. The retrieved solid was sequentially washed by DI water and ethanol, followed by air-drying at 105°C for 12 h, to form the template. Then, 0.3 g template and 7.28 g $\text{Bi}(\text{NO}_3)_3 \cdot 5\text{H}_2\text{O}$ were dispersed in 60 mL DI water under sonication. The suspension was sealed in autoclave and heat-treated at 160°C for 6 h. The retrieved solid was washed by DI water for several times and then air-dried at 105°C for 12 h. Bi_2O_3 nanospheres were obtained after calcining the powder at 400°C for 1 h. To prepare the GDE, 10 mg Bi_2O_3 powders, 5 mg carbon black and 100 μL 5 wt% Nafion solution were mixed in a solution containing 1 mL ethanol and 1 mL DI water. 210 μL of catalyst ink was infiltrated into the carbon matrix (Sigracet 29 BC, $1 \times 1 \text{ cm}^2$) to form the catalyst layer of a GDE.

Preparation of Co_3O_4 electrode. To prepare the Co_3O_4 electrode for OER, we used the solvothermal method to grow Co_3O_4 nanostructures on Ni foam. The solution contained 2.7 mmol $\text{Co}(\text{NO}_3)_2 \cdot 6\text{H}_2\text{O}$, 2.7 mmol NH_4F , 13.5 mmol $(\text{NH}_2)_2\text{CO}$ and 30 mL DI water. Then, the acid-washed and cleaned Ni foam ($2 \times 2 \text{ cm}^2$), together with the solution, were sealed in a 50 mL Teflon-lined autoclave. The autoclave was heated up in an oven and maintained at the temperature of 120°C for 6 h. The obtained Ni foam was washed by deionized water for several times and then dried at 50°C . The dried electrode was finally calcined at 300°C to convert the deposited Co species into Co_3O_4 . The sample was denoted as $\text{Co}_3\text{O}_4\text{-Ni}$.

Cell assembly

Other than specified, the custom-built cell comprised three electrodes: a GDE for CO_2RR ($1 \times 1 \text{ cm}^2$), a $\text{Ni}(\text{OH})_2/\text{NiOOH}$ mediator supported on Ni foam ($2 \times 2 \text{ cm}^2$), and a Pt/C GDE ($1 \times 1 \text{ cm}^2$, Pt loading: 0.1 mg cm^{-2}) for HOR. A 1.5 cm thick polyether ether ketone (PEEK) frame was placed between the CO_2RR GDE and the $\text{NiOOH}/\text{Ni}(\text{OH})_2$ mediator, where a Hg/HgO reference electrode (RE) was placed. The mediator and HOR GDE were separated by a 130- μm -thick porous separator ($3 \times 3 \text{ cm}^2$, wet-laid nonwoven fabric by polyolefin). The separator was soaked in 1 M KOH for 24 h before use. The schematics and photograph of the cell are shown in the Supplementary Information.

Materials characterizations

The XRD patterns were recorded by the Rigaku Smartlab X-ray diffractometer using $\text{Cu K}\alpha$ radiation at 40 kV and 44 mA. The SEM images were obtained using the Hitachi-S4800. O_2 production was monitored via the differential electrochemical mass spectrometry (DEMS) system (Shanghai LingLu Instrument Corp., Ltd., China) containing a PrismaPlus quadrupole mass spectrometer from Pfeiffer Vacuum and a custom-built Swagelok cell. Gas product was quantified using a gas chromatography (GC-2014C, Shimadzu, Kyoto, Japan) equipped with a thermal conductivity detector and two flame ionization detectors. Liquid product was quantified by a 600 MHz nuclear magnetic resonance spectrometer (NMR, AVANCE NEO 600). The specific surface area was measured with a Micromeritics ASAP-2020 instrument and analyzed by the Brunauer-Emmett-Teller (BET) method. The Fourier transform infrared (FTIR) spectroscopy was performed on a Nicolet iS10 FT-IR spectrometer.

Electrochemical measurement

Three-electrode test. Other than specified, all electrochemical measurements were conducted using a CHI 660E electrochemical workstation (CH Instrument Inc.). A classic H-type cell was used, which consisted of a 25 mL cathodic compartment and a 25 mL anodic compartment separated by a 183- μm -thick proton exchange membrane (PEM, Dupont N117). Before test, the PEM was first immersed into a 5 wt.% H_2O_2 solution at 80°C for 1 h, followed by soaking in DI water for 0.5 h. Then, it was boiled in a 5 wt.% H_2SO_4 solution at 80°C for 1 h, followed by soaking in DI water for 0.5 h. Platinum plate ($1 \times 1 \text{ cm}^2$) and saturated calomel electrode (SCE) were used as the counter and reference electrode, respectively. All reported potentials were converted to the reversible hydrogen electrode (RHE) using the equation below:

$$E_{\text{RHE}} = E_{\text{SCE}} + 0.059 \times \text{pH} + 0.242 \quad (9)$$

Post iR-compensation was applied at 85% value of the solution resistance which was obtained at open circuit potential using EIS. Before CO_2RR measurement, CO_2 was purged into the 0.1 M KHCO_3 aqueous solution for 30 min. During the CO_2RR test, CO_2 was purged into the cathodic compartment, the measured outlet flow rate was $\sim 27 \text{ mL min}^{-1}$. EIS was recorded at frequencies ranging from 10^5 Hz to 0.01 Hz. ECSA was estimated by measuring an electric double layer capacitance from the scan-rate-dependent CV at various scan rates (20, 40, 60, 80, 100 and 120 mV s^{-1}) in an Ar-saturated 0.5 M Na_2SO_4 electrolyte. The potential window was selected from -0.57 to -0.46 V vs. SCE. The capacitance (C_{dl}) was estimated by plotting the difference of charging current density versus the scan rate.

Both NiOR and NiRR of $\text{Ni}(\text{OH})_2/\text{NiOOH}$ electrode, as well as the OER of Co_3O_4 on Ni foam ($1 \times 1 \text{ cm}^2$) were studied in a three-electrode system. 1 M KOH solution was used as the electrolyte, a platinum plate ($1 \times 1 \text{ cm}^2$) was used as the counter electrode, and a Hg/HgO electrode was used as the reference electrode. LSV and CV was performed at a scan rate of 1 mV s^{-1} . The Tafel slope was calculated using the Tafel equation:

$$\eta = b \log_{10}(j) + a \quad (10)$$

where η , b , and j represent the overpotential, Tafel slope, and current density, respectively. All reported potentials in this section were relative to the RHE using the equation below:

$$E_{\text{RHE}} = E_{\text{Hg/HgO}} + 0.059 \times \text{pH} + 0.098 \quad (11)$$

Post iR-compensation was applied at 85% value of the solution resistance which was obtained at the open circuit potential using EIS.

EIS was carried out at frequencies ranging from 10^5 Hz to 0.01 Hz. The ohmic resistance was not included in the reported Nyquist plots.

Full cell test. In Step 1, CO₂ gas was fed to the cathode with a flow rate of -35 mL min^{-1} and 1 M KOH or 1 M KHCO₃ were supplied to the cell with a flow rate of 20 mL min^{-1} . The polarization curve was obtained at the steady state by biasing the cell at the specific current density for 20 s before recording the cell voltage. No iR compensation was applied in all full cell test. FE of any gas product was calculated by using the following equation:

$$FE(\%) = \frac{F \times z \times \nu \times C_j}{I_{\text{overall}} \times V_m} \quad (12)$$

where F is the Faraday constant (96485 C mol^{-1}), z is the number of electrons transferred to form the CO₂RR product j , ν is the flow rate of supplied gas, C_j is the detected concentration of gas product, I_{overall} is the overall current, and V_m is the molar volume of gas (22.4 L mol^{-1}). FE of liquid products was measured by NMR spectroscopy. The NMR tube contained 0.1 mL of the collected electrolyte solution, 0.1 μL of DMSO as the internal standard and 0.4 mL D₂O. The liquid products were quantified by NMR spectroscopy. According to the NMR spectroscopy, the concentration of liquid product could be obtained through the following equation:

$$C_j = \frac{V_i \times \rho_i}{M_i} \times \frac{S_i}{S_j} \times \frac{m_i}{m_j} \times \frac{1}{\nu_e} \quad (13)$$

where ν_e is the volume of the electrolyte in the NMR tube; $\frac{S_i}{S_j}$ is the ratio of the area of the liquid product peaks to the area of the internal standard peak; $\frac{m_i}{m_j}$ is the ratio of the number of the certain protons in the internal standard to that in the liquid product molecules (m_i is 6 from two methyl groups for DMSO; m_j is 1 for formate); ρ_i is the density of internal standard; V_i is the volume of the internal standard solution in the NMR tube; M_i is the molar mass of the internal standard (M_i is 78.13 g mol^{-1} for DMSO). The FE of liquid product was calculated using the following equation:

$$FE(\%) = \frac{F \times z \times \nu_i \times C_j}{I_{\text{overall}}} \quad (14)$$

where ν_i is the flow rate of the electrolyte. In Step 2, the electrolyte was switched to 6 M KOH and H₂ was fed to the anode with a flow rate of -10 mL min^{-1} .

Poisoning of Pt/C electrode in HOR. The HOR performance of Pt/C was evaluated in a three-electrode system using a glassy carbon rotating-disk electrode (RDE, Pine Instrument, disk area of 0.196 cm^2). 1 M KOH solution with/without 0.1 M methanol, 0.1 M ethanol or 0.1 M formate was used as the electrolyte, respectively. A Pt wire was used as the counter electrode, and a Hg/HgO electrode was used as the reference electrode. The catalyst ink contained 4 mg 20 wt.% Pt/C powder, 950 μL ethanol and 50 μL Nafion solution (5 wt%), and was prepared by ultrasonication. Then, 10 μL catalyst ink was drop-casted onto the glassy carbon electrode, resulting in a catalyst loading of $\sim 0.2 \text{ mg cm}^{-2}$. Before HOR measurements, the electrolyte was bubbled with high-purity H₂ gas for 30 min. Voltammograms were collected at a scan rate of 5 mV s^{-1} at 1600 rpm.

Fabrication and testing of PEMFC

The PEMFC comprises a membrane electrode assembly (MEA) and gas diffusion layers (GDL) on both sides. Commercial Pt/C (57.7 wt% Pt, TKK), isopropanol, and 5 wt% Nafion solution (DuPont, USA) were ultrasonically mixed for 1 h. The resulting ink-like slurry was then sprayed onto the opposite sides of a pretreated sulfonic acid resin

membrane (Dongyue, DF260) as the cathode and anode, respectively. The Pt loadings were 0.5 mg cm^{-2} and 0.1 mg cm^{-2} for the cathode and anode, respectively. The fuel cell was tested with a backpressure of 30 psi at both electrode chamber, and the test temperature was fixed at 70 °C. Both H₂ and O₂ (air) were humidified before feeding into the fuel cell.

Fabrication and testing of AWE

We assembled a zero-gap AWE to evaluate the performance in water splitting¹³. Briefly, the hydrothermally formed Co- and Ni-hydroxides on Ni foam was phosphidated in the atmosphere of PH₃-containing Ar at 300 °C. The obtained Co-Ni phosphide/spinel oxide hybrid nanostructure was super-aerophobic and active for both HER and OER. The electrolyzer comprised two titanium plates as the current collector. Porous polyethersulfone (PES) with a thickness of 0.12 mm was used as the separator. 6 M KOH solution was used as the circulating anolyte and catholyte using a peristaltic pump at 40 rpm. The electrolyte containers and the electrolyzer were submerged in a water bath at 85 °C. The hot water was circulated to avoid overheating of the electrolyzer during operation. No iR compensation was applied.

Fabrication and testing of SOEC

We fabricated an electrode supported SOEC to evaluate the high-temperature water splitting⁵⁴. Briefly, 33 wt% YSZ (yttria stabilized zirconia; TZ-8Y, Tosoh Corporation), 45 wt% NiO and 22 wt% corn starch were mixed in ethanol by ball milling. The retrieved powder was pressed into discs of *ca.* 1.27 cm in diameter and then sintered at 1100 °C for 2 h to obtain strong substrates. We then sequentially applied a functional layer (50 wt% NiO + 50 wt% YSZ, no pore-forming agent) and YSZ electrolyte via spin coating. The half-cell was densified at 1420 °C for 4 h. Finally, the air electrode comprising 50 wt% homemade La_{0.8}Sr_{0.2}MnO_{3-x} and 50 wt% YSZ was applied on the densified electrolyte. In the test, the SOEC button cell was mounted between a pair of co-axile ZrO₂ tube with the fuel electrode sealed by ceramic sealant. The detailed design and photos of the home-built SOEC test setup were shown in Supplementary Fig. 39. The cell was pre-conditioned in 5% H₂ + N₂ at 650 °C to fully reduce NiO into Ni. During water electrolysis, 50% H₂O (steam) + H₂ was fed into the fuel electrode using a mass flow controller and a steam generator. The inlet tube was heated to 105 °C to avoid water condensation. No iR compensation was applied.

Data availability

Source data of Fig. 2, Fig. 4, and Fig. 5 is provided with this paper. Datasets presented in the Supplementary Information are available from the corresponding author on request. Source data are provided with this paper.

References

- García de Arquer, F. P. et al. CO₂ electrolysis to multicarbon products at activities greater than 1 A cm^{-2} . *Science* **367**, 661–666 (2020).
- Zhong, M. et al. Accelerated discovery of CO₂ electrocatalysts using active machine learning. *Nature* **581**, 178–183 (2020).
- De Luna, P. et al. What would it take for renewably powered electrosynthesis to displace petrochemical processes? *Science* **364**, 350 (2019).
- Zhi, W. Y. et al. Efficient electroreduction of CO₂ to C₂-C₃ products on Cu/Cu₂O@N-doped graphene. *J. CO₂ Util.* **50**, 101594 (2021).
- Ma, W. et al. Electrocatalytic reduction of CO₂ to ethylene and ethanol through hydrogen-assisted C–C coupling over fluorine-modified copper. *Nat. Catal.* **3**, 478–487 (2020).
- Ren, S. et al. Molecular electrocatalysts can mediate fast, selective CO₂ reduction in a flow cell. *Science* **365**, 367–369 (2019).

- Lim, C. et al. Enhancement of catalytic activity and selectivity for the gaseous electroreduction of CO₂ to CO: guidelines for the selection of carbon supports. *Adv. Sustain. Syst.* **5**, 2100216 (2021).
- Lu, X. et al. High-performance electrochemical CO₂ reduction cells based on non-noble metal catalysts. *ACS Energy Lett.* **3**, 2527–2532 (2018).
- Kutz, R. B. et al. Sustaination imidazolium-functionalized polymers for carbon dioxide electrolysis. *Energy Technol.* **5**, 929–936 (2017).
- Zheng, T. et al. Large-scale and highly selective CO₂ electrocatalytic reduction on nickel single-atom catalyst. *Joule*, **3**, 265–278 (2019).
- Reyes, A. et al. Managing hydration at the cathode enables efficient CO₂ electrolysis at commercially relevant current densities. *ACS Energy Lett.* **5**, 1612–1618 (2020).
- Zhang, X. Y. et al. In operando identification of in situ formed metalloid zinc³⁺ active sites for highly efficient electrocatalyzed carbon dioxide reduction. *Angew. Chem. Int. Ed.* **61**, e202202298 (2022).
- Li, L. et al. High-rate alkaline water electrolysis at industrially relevant conditions enabled by superaerophobic electrode assembly. *Adv. Sci.* **10**, 2206180 (2022).
- Wang, T. et al. Combined anodic and cathodic hydrogen production from aldehyde oxidation and hydrogen evolution reaction. *Nat. Catal.* **5**, 66–73 (2021).
- Wang, J. et al. Amorphization activated ruthenium-tellurium nanorods for efficient water splitting. *Nat. Commun.* **10**, 5692 (2019).
- Verma, S., Lu, S. & Kenis, P. J. A. Co-electrolysis of CO₂ and glycerol as a pathway to carbon chemicals with improved techno-economics due to low electricity consumption. *Nat. Energy* **4**, 466–474 (2019).
- Wang, L. et al. Regulating the local charge distribution of Ni active sites for the urea oxidation reaction. *Angew. Chem. Int. Ed.* **60**, 10577–10582 (2021).
- Shin, H., Hansen, K. U. & Jiao, F. Techno-economic assessment of low-temperature carbon dioxide electrolysis. *Nat. Sustain.* **4**, 911–919 (2021).
- Xie, K. et al. Eliminating the need for anodic gas separation in CO₂ electroreduction systems via liquid-to-liquid anodic upgrading. *Nat. Commun.* **13**, 3070 (2022).
- Alerte, T. et al. Downstream of the CO₂ electrolyzer: assessing the energy intensity of product separation. *ACS Energy Lett.* **6**, 4405–4412 (2021).
- O'Brien, C. P. et al. Single pass CO₂ conversion exceeding 85% in the electrosynthesis of multicarbon products via local CO₂ regeneration. *ACS Energy Lett.* **6**, 2952–2959 (2021).
- Medvedeva, X. V. et al. Sustainable at both ends: electrochemical CO₂ utilization paired with electrochemical treatment of nitrogenous waste. *Green. Chem.* **22**, 4456–4462 (2020).
- Guo, J.-H. & Sun, W.-Y. Integrating nickel-nitrogen doped carbon catalyzed CO₂ electroreduction with chlor-alkali process for CO, Cl₂ and KHCO₃ production with enhanced techno-economics. *Appl. Catal. B: Environ.* **275**, 119154 (2020).
- Llorente, M. J., Nguyen, B. H., Kubiak, C. P. & Moeller, K. D. Paired electrolysis in the simultaneous production of synthetic intermediates and substrates. *J. Am. Chem. Soc.* **138**, 15110–15113 (2016).
- Martínez, N. P., Isaacs, M. & Nanda, K. K. Paired electrolysis for simultaneous generation of synthetic fuels and chemicals. *New J. Chem.* **44**, 5617–5637 (2020).
- Choi, S. et al. Mechanistic investigation of biomass oxidation using nickel oxide nanoparticles in a CO₂-saturated electrolyte for paired electrolysis. *J. Phys. Chem. Lett.* **11**, 2941–2948 (2020).
- Li, T., Cao, Y., He, J. & Berlinguette, C. P. Electrolytic CO₂ reduction in tandem with oxidative organic chemistry. *ACS Cent. Sci.* **3**, 778–783 (2017).
- Pérez-Gallent, E. et al. Electroreduction of CO₂ to CO paired with 1,2-propanediol oxidation to lactic acid. Toward an economically feasible system. *Ind. Eng. Chem. Res.* **58**, 6195–6202 (2019).
- Na, J. et al. General techno-economic analysis for electrochemical coproduction coupling carbon dioxide reduction with organic oxidation. *Nat. Commun.* **10**, 5193 (2019).
- Yadegari, H. et al. Glycerol oxidation pairs with carbon monoxide reduction for low-voltage generation of C₂ and C₃ product streams. *ACS Energy Lett.* **6**, 3538–3544 (2021).
- Galimova, T. et al. Global demand analysis for carbon dioxide as raw material from key industrial sources and direct air capture to produce renewable electricity-based fuels and chemicals. *J. Clean. Prod.* **373**, 133920 (2022).
- Yan, X. et al. A membrane-free flow electrolyzer operating at high current density using earth-abundant catalysts for water splitting. *Nat. Commun.* **12**, 4143 (2021).
- Vos, R. E. et al. How temperature affects the selectivity of the electrochemical CO₂ reduction on copper. *ACS Catal.* **13**, 8080–8091 (2023).
- Nishimoto, T., Shinagawa, T., Naito, T. & Takanabe, K. Microkinetic assessment of electrocatalytic oxygen evolution reaction over iridium oxide in unbuffered conditions. *J. Catal.* **391**, 435–445 (2020).
- Tan, K. et al. Solid oxide cells with cermet of silver and gadolinium-doped-ceria symmetrical electrodes for high-performance power generation and water electrolysis. *Int. J. Hydrog. Energy* **47**, 25090–25103 (2022).
- Kraglund, M. R. et al. Ion-solvating membranes as a new approach towards high rate alkaline electrolyzers. *Energy Environ. Sci.* **12**, 3313–3318 (2019).
- Jiang, N. et al. Emerging Electrocatalysts for Water Oxidation under Near-Neutral CO₂ Reduction Conditions. *Adv. Mater.* **34**, 2105852 (2021).
- Rosen, J. et al. Electrodeposited Zn dendrites with Enhanced CO selectivity for electrocatalytic CO₂ reduction. *ACS Catal.* **5**, 4586–4591 (2015).
- Won da, H. et al. Highly Efficient, selective, and stable CO₂ electroreduction on a hexagonal Zn catalyst. *Angew. Chem. Int. Ed.* **55**, 9297–9300 (2016).
- Jeon, H. S. et al. Operando evolution of the structure and oxidation state of size-controlled Zn nanoparticles during CO₂ electroreduction. *J. Am. Chem. Soc.* **140**, 9383–9386 (2018).
- Liu, B. et al. Physical and electrochemical characteristics of aluminium-substituted nickel hydroxide. *J. Appl. Electrochem.* **29**, 855–860 (1999).
- Ravikumar, C. R. et al. CuO embedded β-Ni(OH)₂ nanocomposite as advanced electrode materials for supercapacitors. *J. Alloy. Compd.* **736**, 332–339 (2018).
- Wang, L. et al. Fast conversion of redox couple on Ni(OH)₂/C nanocomposite electrode for high-performance nonenzymatic glucose sensor. *J. Solid State Electr.* **19**, 851–860 (2014).
- Chen, W. et al. Nickel-hydrogen batteries for large-scale energy storage. *Proc. Natl Acad. Sci. USA.* **115**, 11694–11699 (2018).
- Xu, L. et al. Plasma-engraved Co₃O₄ nanosheets with oxygen vacancies and high surface area for the oxygen evolution reaction. *Angew. Chem. Int. Ed.* **128**, 5363–5367 (2016).
- Zhao, K. et al. Operando studies of electrochemical denitrogenation and its mitigation of N-doped carbon catalysts in alkaline media. *ACS Catal.* **13**, 2813–2821 (2023).
- Zimmerman, A. *Nickel-Hydrogen Batteries: Principles and Practice* (Aerospace Press American Institute of Aeronautics and Astronautics, Calif. Reston, 2009).
- Cao, X. et al. “Revitalizing” degraded solid oxide fuel cells in sour fuels for bifunctional oxygen catalysis in zinc-air batteries. *Green. Chem.* **22**, 6075–6083 (2020).

49. Friedrich, K. A. et al. CO adsorption and oxidation on a Pt(111) electrode modified by ruthenium deposition: an IR spectroscopic study. *J. Electroanal. Chem.* **402**, 123–128 (1996).
50. Zhang, J., Luo, W. & Züttel, A. Crossover of liquid products from electrochemical CO₂ reduction through gas diffusion electrode and anion exchange membrane. *J. Catal.* **385**, 140–145 (2020).
51. Xia, D. et al. Ultrastable Fe-N-C fuel cell electrocatalysts by eliminating non-coordinating nitrogen and regulating coordination structures at high temperatures. *Adv. Mater.* **35**, e2204474 (2023).
52. Ozden, A. et al. Cascade CO₂ electroreduction enables efficient carbonate-free production of ethylene. *Joule* **5**, 706–719 (2021).
53. Sisler, J. et al. Ethylene electrosynthesis: a comparative techno-economic analysis of alkaline vs membrane electrode assembly vs CO₂-CO-C₂H₄ tandems. *ACS Energ. Lett.* **6**, 997–1002 (2021).
54. Yan, N. et al. Ni-P coated Ni foam as coking resistant current collector for solid oxide fuel cells fed by syngas. *J. Power Sources* **198**, 164–169 (2012).

Acknowledgements

We acknowledge the funding through National Natural Science Foundation of China (52272233, to N.Y.), Guangdong Basic and Applied Basic Research Foundation (2023A1515011161, to N.Y.) and the Netherlands Organization for Scientific Research (NWO) Vidi grant (VI.Vidi.192.045, to N.Y.). Y.S. thanks the funding from Shenzhen Science and Technology Program (JCYJ20220530143401002, to Y.S.). The authors would also like to thank the Center for Electron Microscopy at Wuhan University for support on the microstructural characterizations, Large-scale Instrument and Equipment Sharing Foundation of Wuhan University, Dr. Ran Zhang and Dr. Yucheng Liu from the Core Facility of Wuhan University for their assistance with NMR and SEM analysis, and Prof. Xiangheng Xiao for the support in GC analysis.

Author contributions

X. J. and N. Y. conceived and guided the project. X. J. performed materials synthesis, characterizations, and electrochemical tests. L. K., K. Z. and X. Y. assisted in the cell design and fabrication. H. W. conducted GC analysis. X. C., Y. L. and L. L. performed the AWE test. Y.S. and Z.W. offered materials characterizations and data analysis. D.D.

performed the PEMFC test. X. J. and N. Y. wrote the manuscript with input from all authors.

Competing interests

The authors declare no competing interests.

Additional information

Supplementary information The online version contains supplementary material available at <https://doi.org/10.1038/s41467-024-45787-x>.

Correspondence and requests for materials should be addressed to Ning Yan.

Peer review information *Nature Communications* thanks the anonymous reviewers for their contribution to the peer review of this work. A peer review file is available.

Reprints and permissions information is available at <http://www.nature.com/reprints>

Publisher's note Springer Nature remains neutral with regard to jurisdictional claims in published maps and institutional affiliations.

Open Access This article is licensed under a Creative Commons Attribution 4.0 International License, which permits use, sharing, adaptation, distribution and reproduction in any medium or format, as long as you give appropriate credit to the original author(s) and the source, provide a link to the Creative Commons licence, and indicate if changes were made. The images or other third party material in this article are included in the article's Creative Commons licence, unless indicated otherwise in a credit line to the material. If material is not included in the article's Creative Commons licence and your intended use is not permitted by statutory regulation or exceeds the permitted use, you will need to obtain permission directly from the copyright holder. To view a copy of this licence, visit <http://creativecommons.org/licenses/by/4.0/>.

© The Author(s) 2024